Bioseparation in a Microfluidic Channel Using Magnetic Field Flow Fractionation

Nipu Modak[1], Abhishek Rudra Pal[1], Amitava Datta[2] and Ranjan Ganguly[2]*
[1]Department of Mechanical Engineering, Jadavpur University, Kolkata 700032, India
[2]Department of Power Engineering, Jadavpur University, Salt Lake Campus, Kolkata 700098, India

ABSTRACT

Magnetophoretic field flow fractionation (FFF) is a promising technique for bioseparation in microfluidic channels for micro-total analysis systems (μ-TAS) applications. A numerical study of FFF of magnetic microspheres of two different sizes in a micro-channel under a transverse magnetic field is studied. Due to the difference in the particle magnetophoretic mobility, particles develop different transverse velocities leading to their separation through two different outlets of the microchannel. Capture efficiency and separation index for the particles are computed at the two outlets, and their variations under different parametric conditions, viz., particle size and susceptibility, magnetic dipole strengths and positions, fluid viscosity and flow velocity, are characterized. Parametric studies show that the capture efficiency and separation index figures are high within a very narrow zone of operating conditions. Beyond this regime, the particles are either trapped on the wall before or after their designated outlets (leading to poor capture efficiency), or are getting collected at the non-designated outlet (leading to poor separation index). Therefore, it is important to determine the optimum parametric and operating condition to achieve the best performance of the FFF device for any BioMEMS application.

NOMENCLATURE

a_1, a_2	Radii of larger and smaller particles, respectively (m)
CE_1, CE_2	Capture efficiencies at outlets 1 and 2, respectively
$\hat{e}_r$, $\hat{e}_\phi$	Unit vectors along (r, ϕ,)
$\mathbf{H}$	Magnetic field (Am^{-1})
$\underline{\underline{\mathbf{I}}}$	Unit tensor
K_{wall}	Wall drag multiplier
N_{part}	Particle flux into the channel ($m^{-2}s^{-1}$)
P_1,P_2	Magnitude of dipole strengths near outlets 1 and 2 (A·m)
SI_1, SI_2	Separation index at outlets 1 and 2
u_{max}	Maximum (mid-plane) fluid velocity in the microchannel (ms^{-1})
$\mathbf{V}$	Velocity of fluid (ms^{-1})
$\mathbf{V}_p$	Velocity of particle (ms^{-1})
x_{mag1},x_{mag2}	Horizontal distance of dipoles 1and 2 from inlet plane (m)
y_{mag1},y_{mag2}	Vertical distance of dipoles 1and 2 from outlets 1 and 2 (m)
η	Viscosity of the host fluid (Pa-s)
$\underline{\underline{\tau_V}}$	Stress tensor (N/m^2)
χ_{eff}	Effective susceptibility of magnetic particle
χ_i	Intrinsic susceptibility of magnetic particle

*Corresponding Author: e-mail: ranjan@pe.jusl.ac.in

1. INTRODUCTION

Magnetophoretic isolation of biological cells in a micro-fluidic environment has strong relevance in biomedicine and biotechnology applications. Functionalized magnetic particles offer a viable tool for selective bio-separation as they enjoy several advantages over other modes of micro-fluidic separation techniques:the particles offer strong magnetic contrast in most of the biological media; they can be easily manipulated inside micro-channels using an external magnetic field; small particle size offer large specific binding site for target analytes; the particles (and the attached biological entities) can be detected using magneto-resistance (MR) of magnetic relaxation anisotropy (MARIA) techniques that are amenable to easy implementation on micro-fluidic chips. Therefore, magnetophoretic separation using magnetic microspheres have attracted much attention for applications in μ-TAS devices, e.g. for m-RNA isolation [1], in a variety of biological and biomedical applications including the diagnosis and treatment of diseases [2, 3], and for biosensors. A magnetophoretic trap has the simplest microfluidic design where particles are separated from the host flow stream on the side-wall of the microchannel using a transverse magnetic field. Such a trap design can be used for several magnetic bead-based bioanalytical applications, e.g., protein microarrays [4], DNA sequencing and separation [5], RNA extraction and reverse transcription [6, 7], T-cell capture from blood for PCR analysis [8], simultaneous bioassay [9], PCR-free DNA detection [10] and biosensor [11, 12, 13, 14]. Recently, Bu *et al*. [15] extended the magnetic trap design (comprising an array of small NdFeB permanent magnets arranged into a checkerboard pattern with alternating magnetization directions and an array of integrated permalloy elements encapsulated in the bottom of a microfabricated separation chamber) for high throughput applications. Microfluidic sorter designs have also been proposed in the literature [16, 17, 18, 19], where the a magnetic field near a bifurcated outflow of a microchannel is so applied that the magnetic particles (along with the bead-bound analyte) emerges from one outlet, while the non-target entities come out from the other. Thus a magnetic sorter design offers continuous flow separation of particles in microchannel. Comprehensive reviews of magnetophoretic separation of biological moieties in microfluidic channels have been provided by Pamme [20] and Ganguly and Puri [21].

Although these magnetic separation techniques have shown much promise in microfluidic bioseparation, selective separation of magnetic microspheres (and different target moieties attached to them) in microfluidic devices is challenging. Traditional trap or sorter designs cannot separate magnetic particles of different magnetic mobilities. Giddings [22] first developed the Field Flow Fractionation (FFF) separation technique where a transverse field is applied to a polydisperse fluid suspension flowing through a long and narrow channel and achieved selective separation. Due to the difference in mobility of the particles under the applied force field, particles develop different transverse velocities and segregate at different regions of the flow. FFF method has been used as an effective flow-based separation technique to purify a range of materials including nano- and microparticles [23]. The method works with a family of flexible elution techniques that are capable of simultaneous separation and measurement. Use of different types of forces employing gravitational [24], fluidic [25], acoustic [26], thermal [27], inertial [28], electrostatic [29], optical [30] and magnetic [31] fields to achieve FFF has been discussed in the literature. Kowalkowski *et al*. [32] compared various sub-techniques of FFF. Williams *et al*. [33] have developed an algorithm that employs numerical integration for analysis of FFF data. Qureshi *et al*. [34] have given an overview of the analytical applications of flow field-flow fractionation (FlFFF) on characterization of bio-molecules.

In magnetophoretic FFF (Fig. 1), magnetic bead-analyte conjugates of different magnetophoretic mobilities are segregated along the axial length of the channel — particles with larger magnetophoretic mobility collects at the upstream outlet while particles with lower mobility travels to the downstream outlets. Thus, it is possible to separate two or more types of specific biological entities (e.g., cells, nucleic acid samples, proteins, etc.) in a single flow-through device. Fedotov *et al*. [35] and Latham *et al*. [36] have used magnetic FFF for characterization of micro and nano-particles in liquid media. Pamme *et al*. [31] reported the continuous sorting of magnetic microspheres in a microfluidic magnetic FFF device. Cells were passed through a wide but shallow microfluidic chamber deflected from the flow direction by a transverse magnetic field gradient to achieve a free flow fractionation according to the mobility of the magnetic beads. They extended the same technique

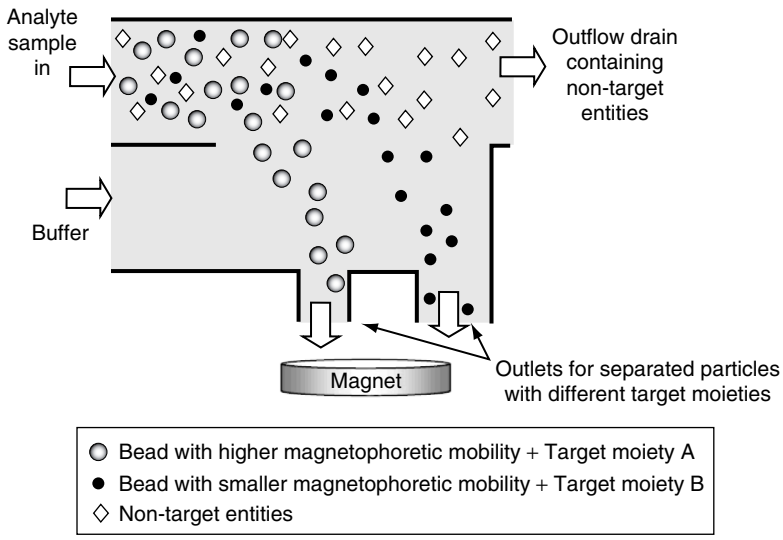

Figure 1. Schematic diagram of the bioseparation principle harnessing magnetophoretic field flow fractionation (FFF).

for separation of magnetic nanoparticles-loaded cells [37]. Although the literature in microfluidic magnetic trap and sorter designs are quite rich, detailed parametric investigations characterizing the performance of FFF design is relatively sparse.

In the present work a comprehensive numerical analysis of magnetophoretic separation that takes into consideration the coupled particle fluid interaction and the requisite channel geometry is presented. An Eulerian-Lagrangian simulation of the fluid flow and particle transport in the microchannel is carried out to characterize the performance of the magnetic FFF device. The trajectories of magnetic beads in a pressure driven flow under the influence of line magnetic dipole is described. The goal is to separate two or more different magnetic microspheres that differ by their properties (such as radius, susceptibility) by varying the particle and fluid parameters and the magnitude of dipole moments so as to capture them in two different outlets. Capture efficiency and separation indices for the particles under different parametric conditions are reported. Optimum conditions for maximum capture efficiency at both outlets are also determined. Findings of the work provides design and operation data of microfluidic magnetophoretic FFF devices.

2. THEORETICAL FORMULATION

Figure 2 describes the flow configuration for the magnetic FFF considered in this paper. A homogeneous suspension of particles having dissimilar magntophretic mobility is released from the upper half of the inlet of the microchannel, while the lower half passes a buffer fluid, separating the background carrier fluid from the outlets. The line dipoles P_1 and P_2 are placed next to the side ports (outlets 1 and 2, respectively) to selectively separate the two magnetic particles – the ones with larger magnetophoretic mobility will come out from the outlet-1, while those with smaller magnetophoretic mobility will come out from the outlet-2. A steady pressure-driven flow is envisaged in the microchannel that carries the particles. The outlet-3 is expected to discharge only the background buffer liquid, and no particles. In a dilute suspension, the magnetic microspheres experience combined magnetic, drag, gravitational, and thermal Brownian forces. The motion of a particle of radius a under these forces is described by applying Newton's second law of motion, i.e.,

$$\left(\tfrac{4}{3}\pi a^3 \rho_p\right) d\mathbf{V}_p/dt = \left[\mathbf{F}_g + \mathbf{F}_m + \mathbf{F}_d + \mathbf{F}_B\right]. \quad (1)$$

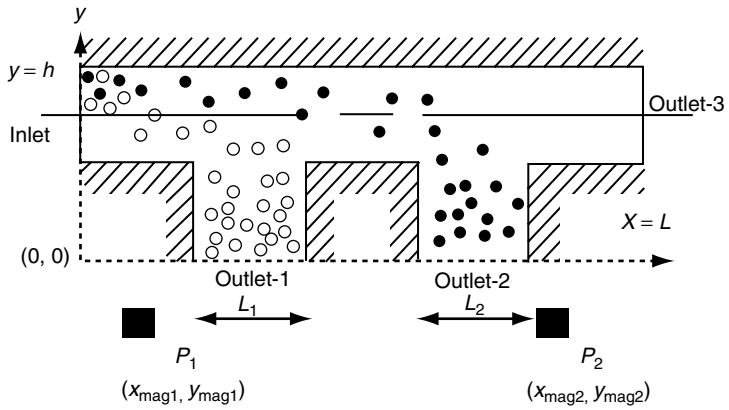

Figure 2. The computational domain and relative positions of the dipoles P_1 and P_2, showing representative separation of magnetic particles with larger (open circles) and smaller (filled circles) magnetophoretic mobility.

The gravity force on a particle of density ρ_p, suspended in a fluid of density ρ, is expressed as $\mathbf{F}_g = \frac{4}{3}\pi a^3\left(\rho_p - \rho\right)\mathbf{g}$. The magnetic and drag forces on the particle clusters are

$$\mathbf{F_m} = \mu_0\left(\frac{4}{3}\pi a^3\right)\chi_{eff}\,\frac{1}{2}\nabla(\mathbf{H}.\mathbf{H}), \text{ and} \tag{2}$$

$$\mathbf{F_d} = K_{wall}6\pi a\eta(\mathbf{V} - \mathbf{V_P}), \tag{3}$$

respectively, where, $\chi_{eff} = \left[\chi_i/\left(1+\frac{1}{3}\chi_i\right)\right]$, and the hydrodynamic drag force is influenced by the presence of walls of the micro-channel. Equation (2) assumes that the particles are not magnetically saturated, so that their magnetization is a linear function of **H**. Dipole-dipole interaction between the magnetized microspheres is also neglected in Eq. (2), since it is a very short-range force, and is not important for dilute suspension of the particles [38]. The wall effect on drag force is incorporated through the wall drag multiplier K_{wall} in Eq. (3). The values of K_{wall} differ while computing the components of drag force parallel and perpendicular to the wall. The corresponding K^p_{wall} and $K^{\perp}_{\text{wall}}$ are calculatedas suggested by Clift *et al.* [39]

$$K^p_{\text{wall}} = \left[1-\frac{9}{16}\xi\right]^{-1}, \text{ and } K^{\perp}_{\text{wall}} = \left[1-\frac{9}{8}\xi\right]^{-1}, \tag{4}$$

Where, ξ denotes the ratio of particle diameter to its distance from the wall. For the particles sufficiently away from the walls, the value of ξ approaches zero, so that the values of K^p_{wall} and $K^{\perp}_{\text{wall}}$ approach unity.

For a microsphere of 1 μm radius (ρ_p = 1,800 kg/m^3) in a fluid having η = 0.001 Pa-s and ρ = 1,000 kg/m^3, a slip velocity of ~1 mm/s produces a Stokesian drag that is nearly 500 times stronger than the gravity force. Moreover, the particle mass being very small (~7.5 × 10^{-15} kg), the inertial effects on the particle trajectories can also be neglected unless the particle acceleration exceeds a very high value [40]. Brownian force on the particle is $\mathbf{F_B} = \mathbf{R_d}\sqrt{12\pi a\eta k_B T/dt}$, where $\mathbf{R_d}$ is a uniform random number vector between 0 and 1, k_B the Boltzmann constant, T the absolute temperature and dt is the time interval over which the Brownian force is resolved. At the time scale of Lagrangian tracking, the Brownian force on the particles can be neglected for particles larger than

40 nm in micro-fluidic environment under magnetic force [41]. The only significant forces that affect the particle motion are, therefore, the magnetic and the viscous drag forces.

Thus, the equation of motion (Eq. 1) for a particle under the combined influences of magnetic and drag forces reduces to:

$$\mathbf{V_P} = V + \mathbf{F_m}/6\pi a\eta\mathbf{K}_{wall}\,. \tag{5}$$

The instantaneous position of a particle cluster can be computed from time integration of the particle velocity, i.e.,

$$X(t) = \int_0^t \mathbf{V}_{PX}\,dt + X_0, \text{ and} \tag{6a}$$

$$Y(t) = \int_0^t \mathbf{V}_{py}\,dt + Y_0 \tag{6b}$$

where (X_0, Y_0) is the initial position of a particle cluster.

The magnetic force on a particle is imposed due to the presence of a pair of line dipoles of strength P_1 and P_2 placed at locations $(x_{\text{mag1}}, y_{\text{mag1}})$ and $(x_{\text{mag2}}, y_{\text{mag2}})$ to produce the necessary magnetic field gradient for particle separation. Figure 2 indicates the locations of the dipoles underneath the lower wall of the channel. Such dipoles can simulate well a two-dimensional magnetic field produced in a practical MEMS device by electromagnets or permanent magnets. Theoretically, a line dipole can be produced by embedding a pair of parallel conductors, carrying currents in opposite directions, next to the microchannel wall. Similar configuration can also be achieved with a much smaller current, by winding multiple turns of conductor around a high aspect ratio magnetic core (with the longer side running perpendicular to the plane of paper) of high permeability materials, e.g., CRGO steel [42]. The magnetic field at any location (r, ϕ) *w.r.t.* the virtual origin of a line dipole is given by the expression [43]:

$$\mathbf{H} = P/r^2(\hat{e}_r \sin\phi - \hat{e}_\phi \cos\phi) = H_r\hat{e}_r + H_\phi\hat{e}_\phi. \tag{7}$$

The combined field can be obtained by superposing the fields obtained by the two dipoles.

Motion of the continuum phase is modelled considering the conservation of mass and momentum in the microchannel and assuming coupled particle–fluid momentum interactions (implying that the particles exert on the fluid a force equal and opposite to the drag, as expressed in Eq. (3), on them). The governing equations are:

$$\frac{\partial\rho}{\partial t} + \nabla.(\rho\mathbf{V}) = 0, \text{ and} \tag{8}$$

$$\frac{\partial}{\partial t}(\rho\mathbf{V}) + \nabla.(\rho\mathbf{V}\mathbf{V}) = -\nabla\mathbf{p} + \nabla.\underline{\underline{\tau}}_v - \lambda\mathbf{F_d}. \tag{9}$$

In Eq. (9), the viscous stress component is denoted by $\underline{\underline{\tau}}_v = \eta[(\nabla V) + (\nabla V)^T] - \frac{2}{3}\eta(\nabla.V)\underline{\underline{\mathbf{I}}}$. The last term in the momentum equation represents the drag force exerted by the particle on the fluid assuming that the suspension is dilute and the particles exert equal and opposite reaction to the drag force exerted on them by the fluid as per Eq. (3).The velocity boundary conditions correspond to plug flow velocity

U_{av} at the inlet, and no-slip along the walls, while the pressure at the outlets is specified to be zero (gauge). Particle cluster concentrations for both the particles at the inlet are also specified.

3. NUMERICAL SIMULATION

Particle-laden flow through the microchannel is solved by an Eulerian-Lagrangian approach. The coupled mass and momentum equations for the liquid phase are solved using a numerical code based on SOLA – an explicit finite-difference technique proposed by Hirt *et al* [44]. The variables (**V** and p) and the fluid properties are described using a staggered grid. The pressure and the fluid properties are specified at the scalar cell centers, while the axial and transverse velocities are specified at the scalar cell faces. The advection and diffusion terms of the transport equations are discretized by hybrid differencing method to avoid numerical diffusion [45]. The time increment for the explicit advancement is calculated by satisfying both the stability criteria and the Courant-Friedrich-Lewy criteria, ensuring that a fluid particle never crosses a complete cell, in either direction, in one time step. Although the solution was sought for a steady-state condition, the code arrived at the final solution by advancing the flow field variables through a sequence of short time-steps.

The particle motion is described by their Lagrangian tracking in the flow-field. A cluster of particles of each type is represented by one representative particle, and its trajectory is found by time-integration of the instantaneous particle velocity given by the Eq. (5). Once the fluid phase is solved for a steady velocity profile using the Eulerian approach, particle tracking is then done in a 'frozen' flow-field. The resulting drag force and its reaction on the fluid is computed, and the fluid phase is solved again, to account for the particle-to-fluid interaction. Particle tracking is done once again in the modified flow field. Detail of the numerical scheme is described elsewhere [40]. The location of each cluster of particles is calculated at every time plane of Lagrangian tracking (i.e. the Eq. 6a and 6b). The momentum source terms (which represent the reaction of the drag force on the particles) are calculated at each vector cell, considering all the particle clusters residing in that cell. A non-uniform grid based on hyperbolic mesh size distribution is used to resolve the sharp gradients near the walls and close to the location of the magnetic dipole. Grid independence is obtained with a 150 × 90 mesh size. The iterative process of fluid and dispersed phases is continued until the difference in the magnitude of drag forces at each cell fall below a preset convergence criterion. The particle trajectories are validated against analytical results of Nandy *et al*. [46] while the capture efficiency data have been compared with the experiments in Modak *et al* [47].

4. RESULT AND DISCUSSION

4.1. Particle trajectories

The flow through the microchannel and the particle trajectories are simulated for different values of operating parameters, e.g., magnetic dipole strength, particle diameter and magnetic susceptibility, fluid viscosity and flow velocity. Table I shows the base values of the operating parameters and the range of parametric variation under which the performance of magnetic FFF device is studied.

For each of these base values and range of parameters, described in Table I, the location of line dipoles are taken as x_{mag1} = 0.0011 m, y_{mag1} = 0.003 m, x_{mag2} = 0.0055 m, y_{mag2} = 0.003 m. For simulation, 100 clusters of each type of particles (having radii a_1 and a_2) are released at the inlet. The number of particles in each cluster is so chosen that a particle influx rate of 5×10^5 $m^{-2}s^{-1}$ is maintained for each type. The trajectories of the particles for the base case can be seen from Fig. 3(a), where the first outlet collects 91 large particle clusters (but no small particles) and the second outlet collects 83 small clusters (but no large particles). The remaining particles are collected on the walls. When the particle sizes are changed, so that a_1 = 2 μm and a_2 = 1 μm, the particles separate in a different fashion. Out of the 100 particle clusters, 91 clusters of the smaller particles are collected at the outlet-1 while all the clusters of the smaller particles are colleted at the upstream outlet 1. The larger particles (marked in blue) have higher magnetophoretic velocity, and are captured more strongly than the smaller (red) particles in both the cases. Therefore, in order to separate the particles, it is expected to capture the larger particles in the first outlet (Outlet 1) of the microchannel and the smaller ones in the second (Outlet 2).

Table 1. The base values and range of variation of operating parameters.

Parameter	Base value(unit)	Range (unit)
a_1	2 (μm)	0.5–6 (μm)
a_2	1 (μm)	0.25–3 (μm)
P_1	3 (A-m)	0.5–4 (A-m, for p_2 = 8 A-m)
P_2	8 (A-m)	3–8 (A-m, for p_1 = 3 A-m)
η	0.001 (Pa-s)	0.0004–0.003 (Pa-s)
χ_1	0.1	0.03–0.3
χ_2	0.1	Fixed at 0.1
u_{max}	0.004 (m/s)	0.001–0.01 (m/s)
x_{mag1}	0.0011 (m)	0.0005–0.0035 (m)
		(excluding 0.001 < x < 0.0025 m)
x_{mag2}	0.0055 (m)	0.0033–0.0059 (m)
		(excluding 0.0035 < x < 0.0049 m)
y_{mag}	0.003 (m)	0.002–0.004 (m)

Channel height: 0.001 m, length: 0.006 m, Outlet 1: 0.0011 m < x < 0.0025 m, outlet-2: 0.0036 m < x < 0.005 m

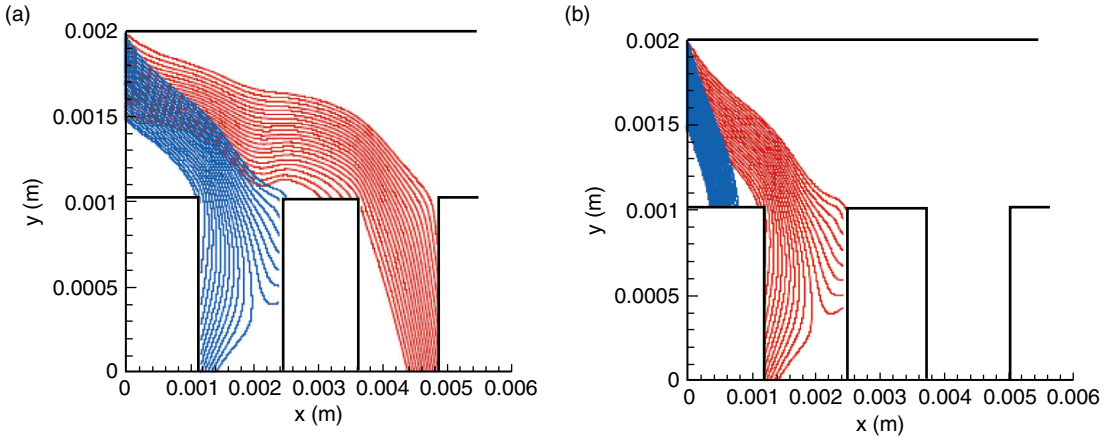

Figure 3. Trajectories of (a) 1 μm (red) and 2 μm (blue) particles for the base case (Table I). x_{mag1} = 1.1 mm, x_{mag2} = 5.5 mm, y_{mag1} = y_{mag2} = 300 μm. (b) Trajectories for 2 μm (red) and 4 μm (blue) radii particles for the same conditions.

4.2. Capture efficiency and separation index

The objective of the device is to collect the maximum number of particles in its designated outlet with as little intermixing between the particles as possible. The device performance is, therefore, defined in terms of capture efficiencies at outlet-1 (CE_1) and outlet-2 denoted (CE_2) as:

$$CE_1 = \frac{\text{Number of larger particles captured at Outlet 1}}{\text{Number of larger particles entering the channel}}, \text{ and} \tag{10a}$$

$$CE_2 = \frac{\text{Number of smaller particles captured at Outlet 2}}{\text{Number of smaller particles entering the channel}}. \quad (10b)$$

It is desired that only the larger particles are captured at outlet-1 and the smaller particles are captured at outlet-2, but there is possibility that both types of particles are captured in either outlets. Therefore, two additional parameters are defined to quantify the extent of segregation of the particles:

$$SI_1 = \frac{\text{Number of larger particles captured at Outlet 1}}{\text{Total number of particles captured at Outlet 1}}, \text{ and} \quad (11a)$$

$$SI_2 = \frac{\text{Number of smaller particles captured at Outlet 2}}{\text{Total number of particles captured at Outlet 2}}. \quad (11b)$$

The device yields a very good performance for the base case (Fig. 3(a)) with $CE_1 = 91\%$, $CE_2 = 83\%$, $SI_1 = SI_2 = 100\%$. On the other hand, for the case of Fig. 3 (b) the capture efficiencies are poor, although some particle capture does take place. For this case, $CE_1 = 0\%$ (no large particle is collected in Outlet 1) and $CE_2 = 0\%$ (no small particle is collected in Outlet 2). For the same reason, both SI_1 and SI_2 are 0%. Therefore, it is evident that any deviation in the operating parameters (e.g., the fluid velocity, viscosity, particle size, magnetic content or the dipole strength) would alter the *CE* and *SI* values.

4.3. Influence of operating and design parameters on *CE* and *SI*

It is necessary to vary each of the parameters described in Table I to find out the operating range between which satisfactory separation and capture of particles are obtained with the device. Each of the parameters, viz. a_1, a_2, P_1, P_2, η, χ_1, χ_2, u_{max}, x_{mag1} and x_{mag2} are varied while keeping the other parameters unchanged, and the device performance is evaluated in terms of CE_1, CE_2, SI_1 and SI_2.

4.3.1. Variation of particle radii (a_1 and a_2)

Figure 4 describes the variation of capture efficiencies and separation indices as functions of the corresponding particle radius. Both the larger and smaller radii are varied keeping the ratio ($r = a_1/a_2$) fixed at a specific value, e.g., $r = 2$ for this case. It is clear from Figure 4(a) that values of CE_1, CE_2 are initially 0% which gradually increases up to the maximum values of $CE_1 = 91\%$ and $CE_2 = 83\%$, and then again gradually decreases to 0%. If the radius of magnetic particle increases, the attractive force

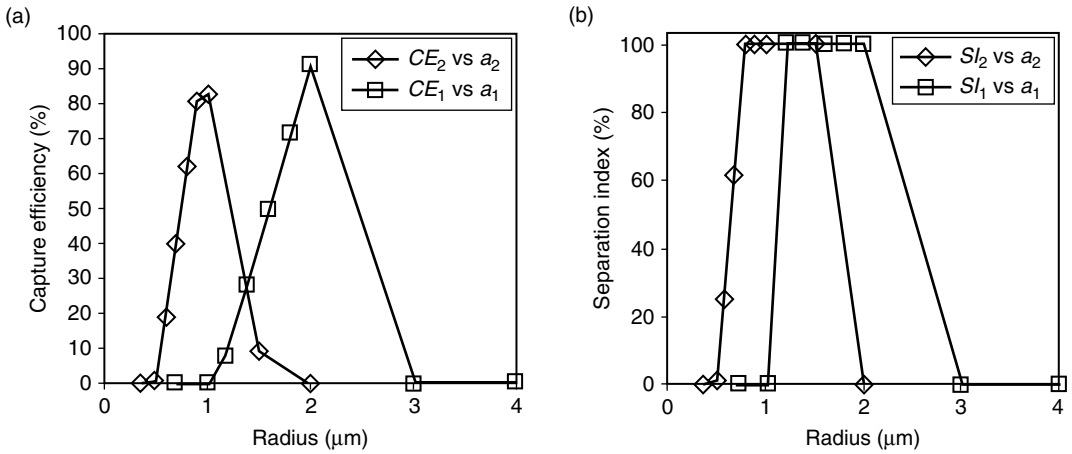

Figure 4. Variation of (a) capture efficiency and (b) separation index for the large and small particles with the radii of the particles for $a_1/a_2 = 2$.

between the dipole and the microsphere also increases proportionately. At a very small radius the magnetic force on the particles is too small to capture them at their desired outlets and particles get carried over with the flow. With the increase in particle radius, magnetic force on the particle also increases and increasing number of particles get captured at the desired outlet increasing the capture efficiency. This trend continues till the threshold radius for which the maximum capture efficiency is observed. With further increase of radius the attractive force causes the particles to get captured at the upstream of the desired outlet causing the capture efficiency to decrease again. Separation indices (SI_1 and SI_2) also show somewhat similar trends in the capture efficiencies. However, the maximum separation index (100%) occurs over a range of particle radius (viz. 0.8 – 1.5 μm for the small particles and 1.2 – 2 μm for the larger one as described in Fig. 4(b)), instead of at a single threshold value. The trend for other combinations of particle radii are observed to be similar, but the exact nature of the *CE* and *SI* curves depend upon the relative forces on the two types of particles admitted into the channel.

4.3.2. Influence of the dipole strengths (P_1 and P_2)

To study the influence of dipole strength on the device performance, P_1 is first varied keeping P_2 fixed at 8 A-m. Next, P_2 is varied keeping P_1 at 3 A-m. The variations of *CE* and *SI* figures are summarized in Fig. 5. From Fig. 5(a) it is seen that while P_1 is increased from 0.5 A-m to 4 A-m,

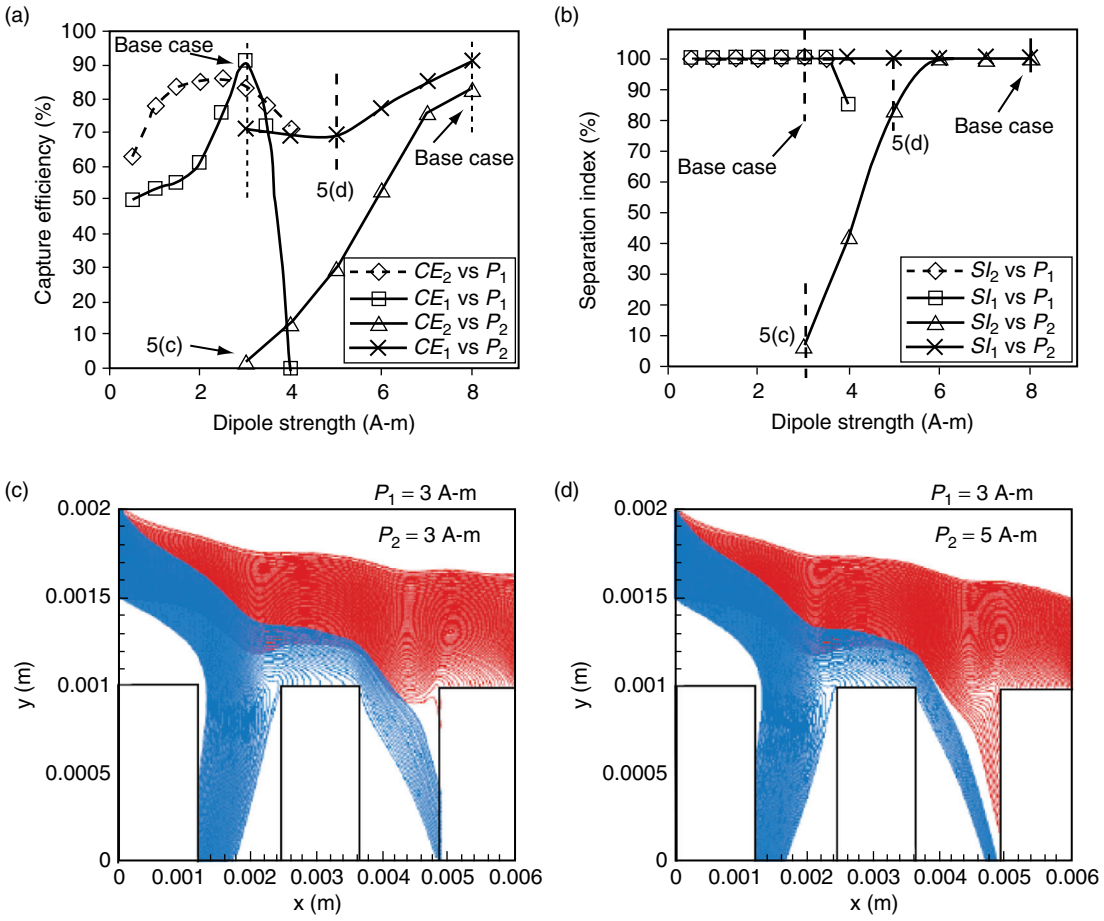

Figure 5. Variation of (a) *CE* and (b) *SI* with dipole strength. Base values of P_1 and P_2 are as per Table 1. Particle trajectories for P_1 = 3 A-m and (c) P_2= 3 A-m, and (d) P_2= 5A-m. The base case condition (Table 1) and conditions corresponding to frames (c) and (d) are marked on frames (a) and (b).

both the CE_1 and CE_2 values first increase, and then decrease. At low P_1 values, some of the larger particles are captured at the downstream of the Outlet 1 while some smaller particles escape from Outlet-3. With increasing P_1, the magnetic attraction on the particles increases both CE_1 and CE_2 at their respective outlets. At larger values of P_1 more particles are trapped before their respective outlets, leading to decline in capture efficiencies. For almost the entire range of P_1 studied here, the *SI* values (Fig. 5(b)) are at 100%, indicating that only larger particles are captured in Outlet 1 and smaller particles are captured in Outlet 2. It is only at P_1 = 4 A-m that the SI_1 drops to about 83% as some of the smaller particles tend to get collected at the Outlet 1. In both Figs 5(a) and (b) the base case combination of P_1 = 3 A-m and P_2 = 8 A-m are marked by the black arrows, signifying high *CE* and *SI* values.

Influences of the dipole strength P_2 on the *CE* and *SI* differ from those due to P_1. For example, for P_1 = 3 A-m, at low values of P_2, the CE_1 is found to stay nearly constant until P_2 = 5 A-m, beyond which it increases. This implies that at large P_2 values, its influence is strong enough to enhance even the capture of larger particles at Outlet 1. The CE_2 value increases monotonically with P_2. For the value of P_1 and the ranges of P_2 chosen in Fig. 5, the Outlet 1 collects only the larger particles, implying SI_1 = 100%. At $P_1 = P_2$ = 3 A-m, 20 number of larger particle clusters are captured along with 2 clusters of small particles in Outlet 2, yielding a poor SI_2. With increased P_2, more number of smaller particles get captured at the Outlet 2. However, for the larger particles, the influence is somewhat counterintuitive. The positions of the dipoles are such (see Table 1) that an increase in P_2 actually pulls down more and more of the larger particles through the Outlet 1. For example, increase of P_2 from 3 A-m to 5 A-m, with P_1 = 3 A-m, changes the particle capture statistics at Outlet 2 from 20 large clusters and 2 small clusters (Fig. 5(c)) to 6 large clusters and 30 small clusters (Fig. 5(d). Beyond P_2 = 6 A-m, no large particle cluster is found to be captured in the second outlet. Thus, with increasing P_2, the SI_2 gradually increases from 6.25% at P_2 = 3 A-m to 100% for $P_2 \geq$ 6 A-m.

4.3.3. Influence of the fluid viscosity (η)

The viscosity of the host fluid can influence the particle trajectories through the drag force on the particles (see Eq. (3)), and therefore, the capture efficiencies and separation indices are expected to depend on the viscosity. Variation of the *CE* and *SI* with the fluid viscosity is plotted in Fig. 6. When the viscosity is very low (e.g., at η = 0.0004 Pa-s) the drag on the particles is so low that particles are captured ahead of their respective outlets. As the viscosity increases, the fluid drag in the axial direction increases and more and more particles are collected at their destined outlets, leading to an initial increase in the capture efficiency. However, with further increase of η (beyond 0.001 Pa-s) particles tend to get washed away in the downstream instead of being collected at their respective outlets. Thus the *CE* value declines with η at higher values of viscosities. A similar trend is observed in the *SI* curves

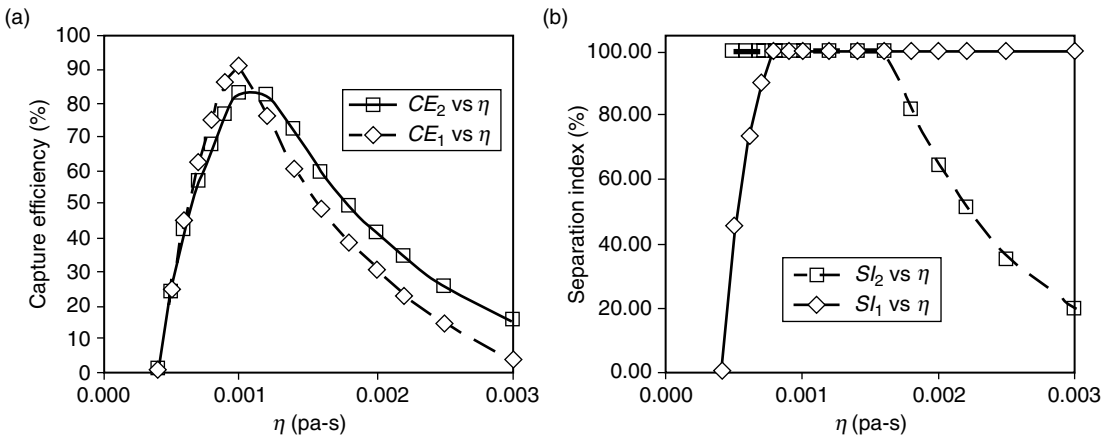

Figure 6. Variation of (a) *CE* and (b) *SI* with viscosity at two different outlets.

(Fig. 6(b)), where the particles are found to collect at their destined outlets, with minimum carryover or carry-under to the other outlet, for a certain range of viscosity. Since the drag force increases equally on both the smaller and the larger particles for a given increase of η, the *CE* and *SI* curves exhibit corresponding trends. Figure 6 suggests that there exists a narrow range of η, when both the *CE* and *SI* figures are simultaneously high, but outside this range the values decrease sharply.

4.3.4. Effect of variation of particle susceptibility (χ_1 and χ_2)

When the magnetic susceptibility of one set of particles (larger or smaller) vary, only the particle trajectories of that type of particles change. Therefore, any change in χ_1 and χ_2 can only influence the CE_1 and CE_2, respectively. Thus, it is obvious that variation of χ_1 does not influence CE_2, while CE_1 remains insensitive to a change in χ_2. Figure 7 shows the variation of *CE* and *SI* figures when the χ_1 and χ_2 are varied separately, keeping the other susceptibility at its base value of 0.1. As can be seen from Fig.7, the CE_1 and SI_2 are very low at lower values of χ_1. At this condition, force on the larger particles is relatively small and some of these particle clusters even collect at the Outlet 2. This causes a low value of SI_2 at small χ_1. With the increase of χ_1, the magnetic force on the larger particle increases, so more of these particle clusters are captured at Outlet 1. Further increase of susceptibility beyond 0.1 causes more of these particle clusters to be collected ahead of outlet-1, leading to a fall in CE_1. Thus, CE_1 shows a high value only in a very narrow range of χ_1. In a similar fashion, the CE_2 also shows a high value in narrow range of χ_2.

4.3.5. Effect of variation of flow velocity (u_{max})

Increasing the flow velocity in the channel leads to higher viscous drag in the *x* direction on the particles. For operating conditions when the particles tend to get captured ahead of their designated outlet (e.g., in the case of Fig. 3(b)), increased flow velocity leads to an increase in the capture efficiency. This is reflected in the lower velocity regime of Fig 8 (a) where the capture efficiencies are plotted as functions of the maximum flow velocity (u_{max}) appearing at the mid-plane of the channel. At low velocity (e.g., at u_{max} = 0.001 m/s), the larger particles are captured ahead of the Outlet 1 and smaller particles collected at the Outlet 1. Thus the CE_1 and CE_2 are zero at this velocity, and the corresponding *SI* values are undefined. Capture efficiency increases with the flow velocity for both the particles till u_{max} = 0.004, beyond which the particles tend to overshoot. The SI_1 values increase with increased flow velocity to 100 % at u_{max} = 0.004 m/s, beyond which no more smaller particles enter the Outlet 1 (Fig. 8(b)). SI_2 value of 100% is observed between 0.004 – 0.006 m/s, beyond which SI_2 again drops down, as the increased viscous drag at higher velocity brings some of the larger particles to the Outlet 2. Therefore, for the parametric conditions as described in Table 1, the *CE* and *SI* values are high in a narrow operating regime.

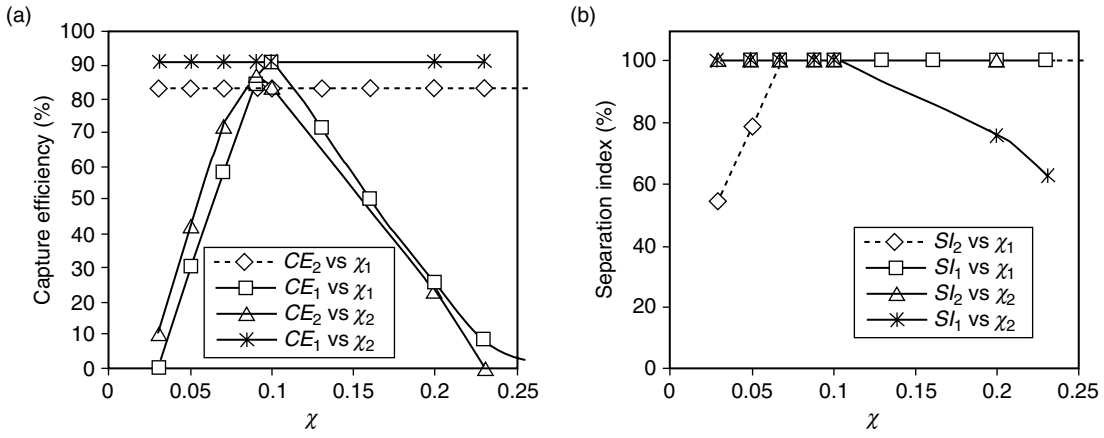

Figure 7. Variation of (a) *CE* and (b) *SI* at two different outlets with the particle susceptibilities. Base values of χ_1 and χ_2.

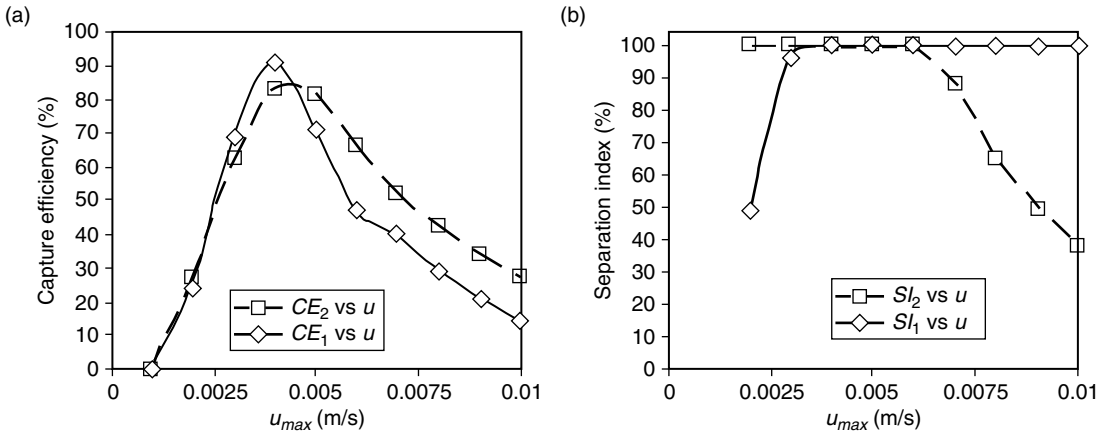

Figure 8. Variation of (a) capture efficiency and (b) separation index with the average flow velocity.

5. CONCLUSIONS

Transport and magnetic field flow fractionation (FFF) of two different-sized magnetic microparticles in a microfluidic channel is investigated through a numerical simulation using an Eulerian-Lagrangian approach. A pair of line dipoles, placed suitably next to the two side-outlets of the channel, generates the necessary magnetic field gradient for selective magnetophoretic capture of magnetic beads. At a given strength of magnetic field gradient the magnetic force on the larger particles exceed that on the smaller ones. This feature is harnessed to design an FFF device that captures the larger particles at the upstream outlet (outlet -1) and the smaller particles in the downstream outlet (outlet-2) of the channel. Particle trajectories are compared for different combinations of particle radii. Capture efficiency of the particles at their designated outlets are evaluated under different working conditiolns, viz., particle size and susceptibility, magnetic dipole strengths, fluid viscosity and flow velocity. The extent of separation of the two particles at each outlet is also evaluated in terms of the separation indices. The simulations show that for operating conditions when the magnetic force on the particles is stronger than an optimum value, particles are trapped on the channel wall ahead of their designated outlets. This leads to poor values of CE_1 and CE_2. Also smaller particles show a trend of getting captured at the Outlet 1, leading to poor separation index at this outlet. The reverse happens when a relatively weak magnetic force on the particles lead to escape of the particles or their capture at the downstream of their designated outlets. Such conditions also lead to carryover of the larger particles to the Outlet-2, leading to low separation index there. The operating regime for which the *CE* and the *SI* values at both the outlets are high is observed only for a very narrow range of the parameters. Thus, the study provides the optimum parametric conditions to achieve the best performance of the FFF device for any bioseparation application.

REFERENCE

[1] Jiang G, and Harrison DJ, mRNA isolation in a microfluidic device for eventual integration of cDNA library construction, *Analyst*, 2000, 125, 2176–2179.

[2] Whitesides GM, Kazlauskas RJ, and Josephson L, Magnetic separations in biology, Trends *Biotechnol*., 1983, 1, 144–148.

[3] McCloskey KE, Chalmers JJ, and Zborowski M, Magnetic cell separation: characterization of magnetophoretic mobility, *Anal Chem*., 2003, 75, 6668–6874.

[4] Morozov VN, and Morozova TY. Active bead-linked immunoassay on protein microarrays. *Analytica Chimia Acta*., 2006,564, 40–52.

[5] Doyle PS, Bibette J, Bancaud A, and Viory J-L, Self-assembled magnetic matrices for DNA separation chips, Science, 2002, 295, 2237.

[6] Jiang G, and Harrison DJ, mRNA isolation in a microfluidic device for eventual integration of cDNA library construction, *Analyst*., 2000, 125, 2176–2179.

[7] Liu C-J, Lien KY, Weng CY, Shin JW, Chang TY, and Lee GB, Magnetic-bead-based microfluidic system for ribonucleic acid extraction and reverse transcription processes, *Biomed. Microdevices*., 2008, 11, 339–350.

[8] Furdui VI, and Harrison DJ, Immunomagnetic T cell capture from blood for PCR analysis using microfluidic systems, *Lab Chip*, 2004, 4, 614–618.

[9] Bronzeau S, and Pamme N, Simultaneous bioassays in a micro- fluidic channel on plugs of different magnetic particles. *Anal. Chimia Acta*, 2008, 609, 105–112.

[10] Dubus S, Gravel JF, Drogoff BLe, Nobert P, Veres T, and Boudreau D, PCR-free DNA detection using a magnetic bead supported polymeric transducer and microelectromagnetic traps. *Anal. Chem*., 2006, 78, 4457–4464.

[11] Graham DL, Ferreira HA, and Freitas PP, Magnetoresistive-based biosensors and biochips, *Trends Biotechnol*., 2004, 22, 455–462.

[12] Goral VN, Zaytseva NV, and Baeumner AJ, Electrochemical microfluidic biosensor for the detection of nucleic acid sequences, *Lab Chip*, 2006, 6, 414–421.

[13] Kwakye S, and Baeumner A, A microfluidic biosensor based on nucleic acid sequence recognition, *Anal. Bioanal.Chem*., 2003, 376, 1062–1068.

[14] Zaytseva NV, V.N. Goral, R.A. Montagnab, and A.J. Baeumner. Development of a microfluidic biosensor module for pathogen detection, *Lab Chip*, 2005, 5, 805–811.

[15] Bu M, Christensen TB, Smistrup K, Wolff A, and Hansen MF, Characterization of a microfluidic magnetic bead separator for high-throughput applications, *Sens. Actuators*, A, 2008, 145–146, 430–436.

[16] Rong, R., J.W. Choi, and C.H. Ahn. An on-chip magnetic bead separator for biocell sorting, *J. Micromech*. Microeng., 2006, 16, 2783–2790.

[17] Pekas N, Gragner M, Tondra M, Popple A, and Porter MD, Magnetic particle diverter in an integrated microfluidic format, *J. Magn. Magn. Mater*., 2005, 293, 584–588.

[18] Inglis DW, Riehn R, Austin RH, and Sturm JC, Continuous microfluidic immunomagnetic cell separation, *Appl. Phys. Lett*., 2004, 85, 5093–5095.

[19] Kim KS, and Park J-K, Magnetic force-based multiplexed immunoassay using superparamagnetic nanoparticles in microfluidic channel, *Lab Chip*, 2005, 5, 657–664.

[20] Pamme N, Continuous flow separations in microfluidic devices, *Lab Chip*, 2007, 7(12), 1644–1659.

[21] Ganguly R, and Puri IK, Microfluidic transport in magnetic MEMS and bioMEMS. Wiley Interdisciplinary Reviews: Nanomedicine and Nanobiotechnology, 2010, 2(4), 382–399.

[22] Giddings JC, Field-flow fractionation: Analysis of macromolecular, colloidal, and particulate materials, *New Series*, 1993, 260(5113), 1456–1465.

[23] Schimpf ME, Caldwell K, and Giddings JC. Field Flow Fractionation Handbook, Wiley-IEEE, 2000.

[24] Huh D, Bahng JH, Ling YB, Wei HH, Kripfgans OD, Fowlkes JB, Grotberg JB, and Takayama S, Gravity-driven microfluidic particle sorting device with hydrodynamic separation amplification, *Anal. Chem*., 2007, 79, 1369–1376.

[25] M. Yamada, M. Nakashima and M. Seki, Pinched flow fractionation: continuous size separation of particles utilizing a laminar flow profile in a pinched microchannel, *Anal, Chem*., 2004, 76, 5465–5471.

[26] Petersson F, Åberg L, SwÑrd-Nilsson A-M, and Laurell T, Free flow acoustophoresis: microfluidic-based mode of particle and cell separation, *Anal. Chem*., 2007, 79 (14), 5117–5123.

[27] Sant HJ, and Galeb BK. Optimization and characterization of a microscale thermal field-flow fractionation system, *Sensors and Actuators B: Chemical*, 2012, 162(1), 223–228

[28] Dutz S, Hayden ME, Schaap A, Stoeber B, and Häfeli U, A microfluidic spiral for size-dependent fractionation of magnetic microspheres. *J. Magn. Magn. Mater., 2012*, 324, 3791–3798.

[29] Čemažar J, Kotnik T, Dielectrophoretic field-flow fractionation of electroporated cells. *Electrophoresis*, 2012, 33(18), 2867–2874.

[30] MacDonald MP, Spalding GC, and Dholakia K, Microfluidic sorting in an optical lattice, *Nature*, 2003, 426, 421–424.

[31] Pamme N, Eijkel JCT, and Manz A On-chip free-flow magnetophoresis: Separation and detection of mixtures of magnetic particles in continuous flow, *J. Magn. Magn. Mater*., 2006, 307, 237–244.

[32] Kowalkowski T, Buszewski B, Cantado C, and Dondi F, Field-flow fractionation: Theory, techniques, application and the challenges, *Critical Rev. Anal. Chem*., 2006, 36 (2), 129–35.

[33] Williams JPS, Giddings MC, and Giddings JC, A data analysis algorithm for programmed field-flow fractionation, *Anal Chem*., 2001, 73(17), 4202–4211.

[34] Qureshi RN, and Kok WT, Application of flow field-flow fractionation for the characterization of macromolecules of biological interest, a review, *Anal Bio-anal Chem*., 2011, 399(4), 1401–1411.

[35] Fedotov PS, Vanifatova NG, Shkinev VM, and Spivakov BY, Fractionation and characterization of nano and microparticles in liquid media, *Anal Bioanal Chem*., 2010 400(6), 1787–1804.

[36] Latham AH, Freitas RS, Schiffer P, and Williams ME, Capillary magnetic field flow fractionation and analysis of Magnetic Nanoparticles. *Anal. Chem*., 2005, 77 (15), 5055–5062.

[37] Pamme N, and Wilhem C, Continuous sorting of magnetic cells via on-chip free-flow magnetophoresis, Lab Chip, 2006, 6, 974–980.

[38] Ganguly R, and Puri IK, Field-assisted Self Assembly of Superparamagnetic Nanoparticles for Bio-medical, MEMS and BioMEMS Applications. Adv. Appl. Mech., 2007, 41, 293–335.

[39] Clift R, Grace JR, Weber ME, Bubbles drops, and particles. Academic press, New York, 1978.

[40] Modak N, Datta A, and Ganguly R, Cell separation in a microfluidic channel using magnetic microspheres, *Microfluid. Nanofluid*., 2009, 6(5), 647–660.

[41] Furlani EP, Analysis of particle transport in a magnetophoretic microsystem. *J. Appl. Phys*., 2006, 99, 024912(1–11).

[42] Fink DG, Standard handbook for electrical engineering. McGraw Hill, New York, 1969.

[43] Ganguly R, Sen S, and Puri IK, Heat transfer augmentation in a channel with a magnetic field under the influence of a line-dipole. *J. Magn. Magn. Mater*., 2004, 271, 63–73.

[44] Hirt CW, Nicols BD, and Romero NC, Los Alamos Scientific Laboratory Report LA-5852 Los Alamos New Mexico, 1975.

[45] Patankar SV, Numerical Heat Transfer and Fluid Flow. Washington, Hemisphere Publishing Corporation, 1980.

[46] Nandy K, Choudhury S, Ganguly R, and Puri IK, Analytical model for the magnetophoretic capture of magnetic microspheres in microfluidic devices, *J. Magn. Magn*. Mater. 2008, 320(7), 1398–1405.

[47] Modak N, Kejriwal D, Nandy K, Datta A, and Ganguly R, Experimental and numerical characterization of magnetophoretic separation for MEMS-based biosensor applications, *Biomed. Microdev*., 2010, 12(1), 23–34.